Volume 10
Number 8
28 February 2022
Pages 2855–3262

Journal of Materials Chemistry C

Materials for optical, magnetic and electronic devices

rsc.li/materials-c

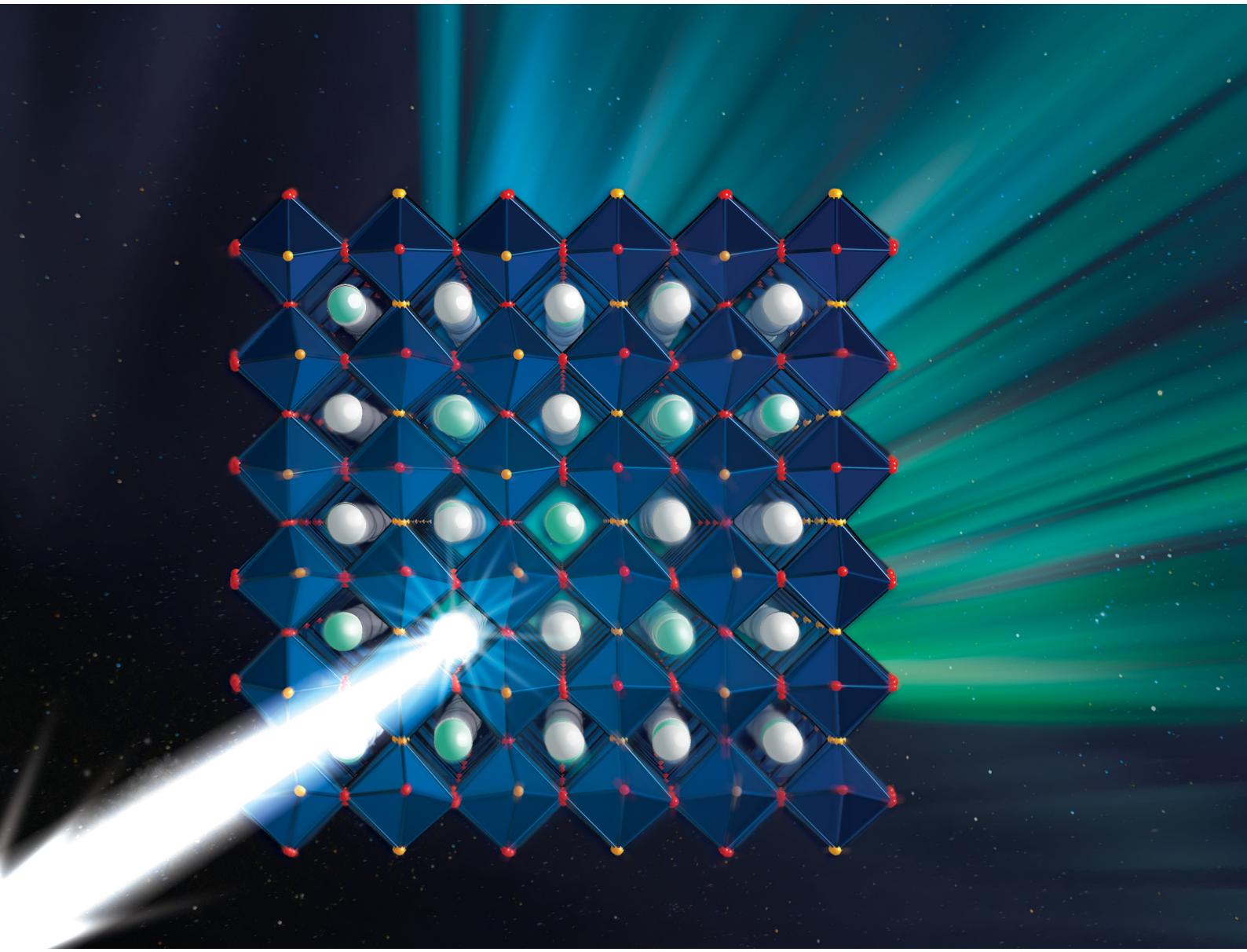

ISSN 2050-7526

ROYAL SOCIETY OF CHEMISTRY

PAPER

Jakoah Brgoch *et al.*

Local environment rigidity and the evolution of optical properties in the green-emitting phosphor $Ba_{1-x}Sr_xScO_2F:Eu^{2+}$

Journal of Materials Chemistry C

ROYAL SOCIETY OF CHEMISTRY

PAPER

View Article Online
View Journal | View Issue

Cite this: J. Mater. Chem. C, 2022, 10, 2955

Local environment rigidity and the evolution of optical properties in the green-emitting phosphor $Ba_{1-x}Sr_xScO_2F:Eu^{2+}$†

Shruti Hariyani, ‡[ab] Mahdi Amachraa, ‡[c] Mariam Khan,[a] Shyue Ping Ong [c] and Jakoah Brgoch *[ab]

Received 9th November 2021,
Accepted 28th January 2022

DOI: 10.1039/d1tc05411b

rsc.li/materials-c

Developing chemically and thermally stable, highly efficient green-emitting inorganic phosphors is a significant challenge in solid-state lighting. One accessible pathway for achieving green emission is by forming a solid solution with superior blue-emitting materials. In this work, we demonstrate that the cyan-emission (λ_{em} = 481 nm) of the $BaScO_2F:Eu^{2+}$ perovskite can be red-shifted by forming a solid solution following $(Ba_{1-x}Sr_x)_{0.98}Eu_{0.02}ScO_2F$ (x = 0, 0.075, 0.15, 0.25, 0.33, 0.40). Although green emission is achieved (λ_{em} = 516 nm) as desired, the thermal quenching (TQ) resistance is reduced, and the photoluminescence quantum yield (PLQY) drops by 65%. Computation reveals the source of these changes. Surprisingly, a basic density functional theory analysis shows the gradual Sr_{Ba} substitution has negligible effects on the band gap (E_g) energy, suggesting the activation energy barrier for the thermal ionization quenching remains unchanged, while the nearly constant Debye temperature indicates no loss of average structural rigidity to explain the decrease in the PLQY. Instead, temperature-dependent *ab initio* molecular dynamics (AIMD) simulations show that gradual changes of the Eu^{2+} ion's local coordination environment rigidity are responsible for the drop in the observed TQ and PLQY. These results express the need to computationally analyze the local rare-earth environment as a function of temperature to understand the fundamental origin of optical properties in new inorganic phosphors.

1. Introduction

Lighting alone accounts for a disturbing 15% of global energy consumption. Fortunately, solid-state, light-emitting diode (LED) driven light bulbs are quickly becoming an accessible and affordable method to increase energy savings dramatically. Not only are solid-state lighting devices 75% more efficient than incandescent and halogen bulbs, but they also do not contain toxic mercury like compact fluorescent light bulbs.[1] These devices use a semiconducting LED chip to convert electricity to a nearly monochromatic saturated light that is used to excite a phosphor coating on the chip's surface. The most straightforward solid-state light bulb comprises a blue InGaN LED chip ($\lambda_{em} \approx$ 450 nm) and rare-earth activator ion substituted yellow-emitting phosphor, like $Y_3Al_5O_{12}:Ce^{3+}$. The combination of blue and yellow emissive light appears as white.[2] While affordable, the white light produced by these devices contains a "blue spike" from the LED emission, a cyan gap between the blue and green regions of the visible spectrum, and lacks an explicit red spectral component. These spectral qualities lead to the notorious blue-hue that plagues LED light bulbs. These lights also have links to circadian disruption, poor color rendering, and high correlated color temperatures.[3–5] An alternative method proposed to create white light while maintaining the color quality required for general illumination is to utilize UV-LED ($\lambda_{em} \approx$ 365 nm) or violet LED ($\lambda_{em} \approx$ 400 nm) chips coated with a tricolor (red-, green-, and blue-emitting) phosphor mixture.[6] The major limitation preventing the widespread application of this approach is the availability of suitable phosphors. These materials must strongly absorb the higher energy LED light, possess a high photoluminescent quantum yield (PLQY), and have a thermally robust photon emission. Driven by this need, extensive research has developed highly efficient and thermally stable red- and blue-emitting materials, but there is a noticeable gap in the number of viable green-emitting materials. Thus, a current obstacle facing the complete conversion to high-quality solid-state lighting devices driven by UV or violet LEDs is the access to green-emitting phosphors.

Most current green-emitting phosphors possess at least one major drawback that prevents their ubiquitous use in UV-LED driven solid-state light bulbs. The most popular green-emitting

[a] Department of Chemistry, University of Houston, Houston, Texas 77204, USA. E-mail: jbrgoch@uh.edu
[b] Texas Center for Superconductivity, University of Houston, Houston, Texas, 77204, USA
[c] Department of NanoEngineering, University of California San Diego, La Jolla, California 92093, USA

† Electronic supplementary information (ESI) available. See DOI: 10.1039/d1tc05411b
‡ These authors contributed equally to this work.

phosphor, β-SiAlON:Eu^{2+}, is efficient and thermally stable under UV excitation. This phosphor has historically been used in display applications due to its narrow emission full width at half maximum (fwhm) of 54 nm (1760 cm^{-1}).[7] Unfortunately, the narrow green emission band maintains the cyan gap in a white light spectrum. $Lu_3Al_5O_{12}$:Ce^{3+} is more often used as the green-emitter for general illumination due to its broad emission spectrum (fwhm = 103 nm, 3474 cm^{-1}); however, it is not suitable for UV-driven devices due to its poor UV absorption.[8] In contrast, Eu^{2+} substituted orthosilicates, M_2SiO_4:Eu^{2+} (M = Ba, Sr, Ca), are a popular class of materials that emit in the 500–600 nm range under UV excitation. Among these, $Ba_{1.14}Sr_{0.86}SiO_4$:Eu^{2+} possess the highest PLQY of 89% and has been utilized in commercial applications, but this phosphor still suffers from poor thermal stability at elevated temperatures.[9,10] These examples illustrate the critical need to develop new highly efficient, thermally stable, and UV-LED compatible green-emitting phosphors with an emission band broad enough to cover the cyan region of the visible spectrum.

Creating new suitable green-emitting phosphors is incredibly challenging because humans' peak spectral sensitivity lies within the green region of the visible spectrum. As a result, subtle changes in the chromaticity of a green-emitting phosphor from external stimuli such as temperature are highly perceptible to the average human eye and can preclude a material from lighting applications.[11] One approach for creating new thermally and chromatically stable green-emitting phosphors is to increase the rare-earth crystal field splitting of an exemplary blue or cyan-emitting material. Crystal field splitting can be tuned by changing the bond lengths around the rare-earth ions in phosphors, inducing high distortion indices, or changing the rare-earth coordination number.[12] Chemical substitution can also influence a rare-earth ion to selectively occupy a certain substitution site with higher crystal field splitting effects. For example, the substitution of Li^+ on the Al^{3+} site in $NaAlSiO_4$:Eu^{2+} forces the rare-earth ion to selectively occupy the smaller Na(1) site over the larger Na(2) site which red-shifts the observed emission.[12] Another way to increase the crystal field splitting of a phosphor and red-shift the emission maximum is to form a solid solution by substituting a smaller, chemically similar atom in the host crystal structure to shorten the activator-ligand bond length.[13] For example, $Ba_5SiO_4Cl_6$:Eu^{2+} is a well-known narrow-emitting, efficient, and thermally stable blue-emitting phosphor. Incrementally substituting F^- for Cl^- in $Ba_5SiO_4Cl_{6-x}F_x$:Eu^{2+} showed highly tunable luminescence as a function of composition where the blue emission is red-shifted from 440 nm (x = 0) to ≈500 nm when x = 6, producing a green emission. The excitation band of the parent phosphor also red-shifts, allowing the $Ba_5SiO_4Cl_{6-x}F_x$:Eu^{2+} phosphor to be more readily excited by a UV-LED.[14,15] Elemental substitution has also been reported to improve the chemical and structural stability of a phosphor and produce a color-tunable emission. For instance, the solid solution between the nearly isostructural $Sr_2Ba(AlO_4F)$:Ce^{3+} and Sr_3SiO_5:Ce^{3+} increased the phosphor's moisture resistance, allowing it to be more viable for device integration.[16–18] Similarly, an increase in the PLQY and thermal stability of $Ba_2Y_5B_5O_{17}$:Ce^{3+} was obtained by substituting the larger Y^{3+} for the smaller, chemically harder Lu^{3+}, which increased the overall rigidity of the structure as indicated by a ≈20 K increase in the Debye temperature (Θ_D).[19] This indicates that a solid solution is a viable strategy to modify the average structure of a crystalline host material, in turn creating phosphors with tunable optical properties.

One intriguing cyan-emitting phosphor that may benefit from this approach is the recently reported perovskite-based $BaScO_2F$:Eu^{2+}. This phosphor, which follows the $A^{2+}B^{3+}[X^{2-}]_2[Y^-]$ general formula, can be obtained from a straightforward one-step synthetic route. Upon UV excitation, the product produces a broad emission (λ_{em} = 481 nm, fwhm = 103 nm).[20] The full width at half maximum and position of the emission band makes this phosphor ideal for covering the cyan gap. In addition, this phosphor possesses a high PLQY (80%) stemming from the dense connectivity of the perovskite crystal structure. Indeed, the rigid framework of corner-connected $[Sc(O/F)_6]$ octahedra gives rise to a high Debye temperature of 517 K.[20] Unfortunately, this phosphor is not yet suitable for device integration due to its insufficient thermal stability. $BaScO_2F$:Eu^{2+} loses 50% of its low temperature (80 K) integrated emission intensity at 387 K, which is below the US. Department of Energy's expectations (423 K).[21] Nevertheless, the addition of a smaller, chemically similar atom into the $BaScO_2F$ crystal structure, such as Sr^{2+} or Ca^{2+} for Ba^{2+} or Al^{3+} for Sc^{3+}, may provide the needed improvements to the material's PLQY and thermal stability, while red-shifting the cyan emission to produce a novel green that could allow this material to be included in next-generation UV or violet-based white LEDs.

In this work, the formation and optical properties of the solid solution $(Ba_{1-x}Sr_x)_{0.98}Eu_{0.02}ScO_2F$ (x = 0, 0.075, 0.15, 0.25, 0.33, 0.40) are investigated by a combination of advanced experimental characterizations and computational analysis for general applications. The compounds form pure phase products with an average cubic structure as confirmed through Rietveld refinement. Substituting 2% Eu^{2+} across the solid solution produces a color-tunable emission from cyan (x = 0; λ_{em} = 481 nm) to green (x = 0.40; λ_{em} = 516 nm). Interestingly, the continuous exchange of the Ba^{2+} for Sr^{2+} atoms negatively impacts the phosphor's quantum yield and thermal stability, which challenges the hypothesis that structural rigidity will increase upon the substitution of a smaller atom. First-principles calculations revealed an insignificant change in the host's Debye temperature and band gap as a function of Sr^{2+} concentration, indicating that the overall structural rigidity and auto-ionization photoluminescent quenching mechanism, respectively, are unlikely to be the dominant quenching mechanism. It is only through an analysis of the Eu^{2+} local environment using *ab initio* molecular dynamics simulations (AIMD) as a function of Sr^{2+} substitution that the origin of the optical response is identified.[22] These results indicate that advanced AIMD calculations are invaluable for analyzing the effects of elemental substitution of the local activator environment and providing substantial insight into the optical properties of inorganic phosphors.

2. Methodology

2.1 Experimental procedure

The solid solution $(Ba_{1-x}Sr_x)_{0.98}Eu_{0.02}ScO_2F$ (x = 0, 0.075, 0.15, 0.25, 0.33, 0.40) was synthesized by combining $BaCO_3$ (Johnson Mathey, 99.99%), $SrCO_3$ (Alfa Aesar, 99.99%), BaF_2 (Sigma Aldrich, 99.99%), Sc_2O_3 (Alfa Aesar, 99.99%), and Eu_2O_3 (Alfa Aesar, 99.99%) in the appropriate stoichiometric ratio and grinding in an acetone medium. The mixture was further milled in a high-energy ball mill (Spex 8000M Mixer/Mill) for 100 minutes. Pellets (6 mm) of the mixture were placed in alumina crucibles on a bed of sacrificial powder and fired at 1200 °C for 8 hours under flowing 15% H_2/85% N_2 gas with a heating and cooling rate of 3 °C per minute. Preliminary X-ray powder diffraction (X'Pert PANalytical; Cu Kα, λ = 1.5406 Å) revealed a minor BaF_2 impurity. A majority of the impurity was removed by dispersing each powder in hot deionized water and centrifuging (Dynac centrifuge) for 30 minutes. The water was decanted, and the powders were dried by mixing with acetone and drying on a hot plate at 150 °C for 10 minutes.

The phase purity and crystal structure of $Ba_{0.58}Sr_{0.40}Eu_{0.02}ScO_2F$ was confirmed using 11-BM high-resolution synchrotron powder X-ray diffraction at the Advanced Photon Source (APS) at Argonne National Laboratory. The data were collected at 100 K with a calibrated wavelength of 0.457868 Å. The refinement profile was conducted using the General Structural Analysis System (GSAS) software and the EXPGUI interface.[23] The background was fit with a shifted-Chebyshev function and the peak shapes modeled by the pseudo-Voigt function. The refined crystal structure was visualized using VESTA.[24]

The polycrystalline samples were mixed in a silicon epoxy (United Adhesives) and deposited onto a quartz slide (Chemglass). Room temperature photoluminescent data were collected using a PTI fluorescence spectrophotometer with a 75 W xenon arc lamp for excitation. Temperature-dependent emission spectra were obtained using a Janis cryostat (VPF-100) for a temperature-controlled environment from 80 K to 500 K. The internal PLQY was determined following the method of de Mello *et al.*, with a Spectralon-coated integrating sphere (150 mm diameter, Labsphere) using an excitation wavelength of 340 nm.[25] Luminescent lifetimes were determined using NanoLED N-330 nm (λ_{ex} = 336 nm) LED equipped on the Horiba DeltaFlex Lifetime System.

2.2 Computational procedure

The density functional theory (DFT) calculations were conducted using the plane-wave Vienna *ab initio* Simulation Package (VASP)[22] within the projector-augmented-wave (PAW) method.[23] The generalized gradient approximation Perdew–Burke–Ernzerhof (PBE) functional was used in all calculations.[24] All symmetry-unique configurations of O^{2-}, F^- and Sr^{2+} substitutions in the solid solution of $Ba_{1-x}Sr_xScO_2F$ were enumerated using the algorithm of Hart and Forcade using the interface implemented in the Python Materials Genomics (pymatgen) package.[26] The Brillouin zones were integrated with a k-point grid density of at least 100 k-points per Å^{-3} while the energy cutoff was set to 520 eV. The electronic energy calculations converged within 1×10^{-5} eV. A Brillouin zone k-point grid density of 1000 k-points per atom was used while the remaining parameters were similar to those used by the Materials Project.[27]

Structural optimizations of Eu^{2+}-activated $Ba_{1-x}Sr_xScO_2F$ were conducted under the PBE+U method with a Hubbard U value of 2.5 eV for Eu^{2+}.[28,29] To simulate the low concentrations of Eu^{2+} ($\sim$3.5%) that are often studied experimentally, supercell models with lattice parameters $>$10 Å were constructed. Supercell models with x = 0.09375, 0.15625, 0.25, and 0.3125 were relaxed using energies and forces convergence to within 1×10^{-5} eV and 1×10^{-5} eV Å^{-1}, respectively. The lowest energy Eu^{2+}-substituted configuration was used for all relevant analyses.

Using the Wei *et al.* formalism,[30] the dopant formation energies were computed as follows:

$$E_f = E^D_{tot} - E^P_{tot} - \sum_i n_i \mu_i \quad (1)$$

where E^D_{tot}, E^P_{tot} are the total energies of the lattice with and without dopants, respectively. μ_i is the chemical potential of constituent i and n_i indicates the number of species i being removed or added. Finally, the chemical potentials of each species are based on the 0 K DFT phase diagram.

The Debye temperature, Θ_D, was determined from the spherical average of sound velocity in eqn (2),

$$\Theta_D = \frac{\hbar}{k_B}\left[6\pi^2 V^{\frac{1}{2}} n_a\right]^{1/3} \sqrt{\frac{B_H}{M}} f(\sigma) \quad (2)$$

$$f(\sigma) = \left\{3\left[2\left(\frac{2}{3}\frac{1+\nu}{1-2\nu}\right)^{\frac{3}{2}} + \left(\frac{1}{3}\frac{1+\nu}{1-2\nu}\right)^{\frac{3}{2}}\right]^{-1}\right\}^{1/3} \quad (3)$$

where M is the molar mass, N is the number of atoms, V is the volume of the unit cell, k_B and $\hbar$ are the Boltzmann and Planck's constant, respectively, and $f(\sigma)$ is the value obtained using eqn (3), where σ is the Poisson ratio. The elastic moduli, bulk modulus (B_H), and ν were calculated using the Voigt–Reuss–Hill (VRH) approximations based on the computed elastic tensors (C_{ij}) following the method of Wu *et al.*[31]

Ab initio molecular dynamics (AIMD) simulations under the *NVT* ensemble at 300 K and 500 K with Nose–Hoover thermostats carried out on 2 × 4 × 4 supercells with a constant Eu^{2+} concentration of 3% in $Ba_{1-x}Sr_xScO_2F$. The AIMD simulations were non-spin polarized, and a minimal Γ-centered 1 × 1 × 1 k-point mesh with a time step of 2 fs were used.[32]

3. Results and discussion

3.1 Phase and crystal structure

The structural flexibility of perovskites allows solid solutions to be formed with ease.[33] The powder X-ray diffractograms of $(Ba_{1-x}Sr_x)_{0.98}Eu_{0.02}ScO_2F$ (x = 0, 0.075, 0.15, 0.25, 0.33, 0.40),

plotted in Fig. 1a, indicate the samples are isostructural with the parent phase, $BaScO_2F$ (ICSD no. 105805). The perovskite crystallizes with the average cubic space group $Pm\bar{3}m$ (No. 221).[34] The powder X-ray diffractograms also reveal minor impurities of BaF_2 and Sc_2O_3, marked with a red asterisk and a black dot, respectively. The incremental incorporation of Sr^{2+} in the host perovskite crystal structure is confirmed through the gradual shift of the diffraction peaks to larger angles (yellow dashed line, Fig. 1a) following the substitution of the smaller Sr^{2+} ($r_{12\text{-coord}}$ = 1.44 Å) for the larger Ba^{2+} ($r_{12\text{-coord}}$ = 1.61 Å).[35] This shift in the diffraction peaks is corroborated by a slight, linear decrease in the refined lattice parameters, following Vegard's law of substitution (Fig. S1, ESI†).[36] This confirms the ability of the oxyfluoride perovskite to accommodate Sr^{2+} in the cuboctahedral cavity without inducing large average structural changes. A solubility limit is reached when the Sr^{2+} concentration approaches 40%. All attempts to synthesize $(Ba_{1-x}Sr_x)_{0.98}Eu_{0.02}ScO_2F$ with $x > 0.40$ resulted in major $SrSc_2O_4$ impurities, a known red-emitting phosphor upon Eu^{2+} substitution.[37]

Perovskites are famous for symmetry lowering distortions as a function of compositional change.[38] Therefore, a Rietveld refinement of the solid solution end member, x = 0.40, was performed on high-resolution synchrotron X-ray powder diffraction data to confirm the average cubic crystal structure upon Sr^{2+} substitution. The Eu^{2+} ion was omitted from the refinement due to the low substitution concentration in the sample (2%). The refinement results, provided in Fig. 1b, indicate excellent agreement with the previously published crystal structure of $BaScO_2F$, meaning the average cubic $Pm\bar{3}m$ perovskite structure following the $A^{2+}B^{3+}[X^{2-}]_2[Y^-]$ general structural formula is retained even upon maximum Sr^{2+} substitution. The resulting refined crystal structure data and atomic positions are listed in Table 1 and Table S1 (ESI†), respectively. The refined Sr^{2+} content was 43.3(8)%, agreeing with the nominally loaded 40% concentration. The resulting refined perovskite crystal structure of $Ba_{0.566(2)}Sr_{0.433(8)}ScO_2F$ (Fig. 1c) is composed of corner-connected $[Sc(O/F)_6]$ octahedra. The A^{2+} cation is in cuboctahedral coordination and sits in the cavity produced by the octahedral network. Both Eu^{2+} ($r_{12\text{-coord}}$ = 1.48 Å) and Sr^{2+} ($r_{12\text{-coord}}$ = 1.44 Å) are expected to occupy the cuboctahedral site since their ionic radii are similar to that of Ba^{2+} ($r_{12\text{-coord}}$ = 1.61 Å) and substantially larger than Sc^{3+} ($r_{6\text{-coord}}$ = 0.745 Å).[35] The anion disorder has been previously confirmed through ^{19}F-MAS NMR where a single ^{19}F signal was observed, indicating a single fluoride site.[39]

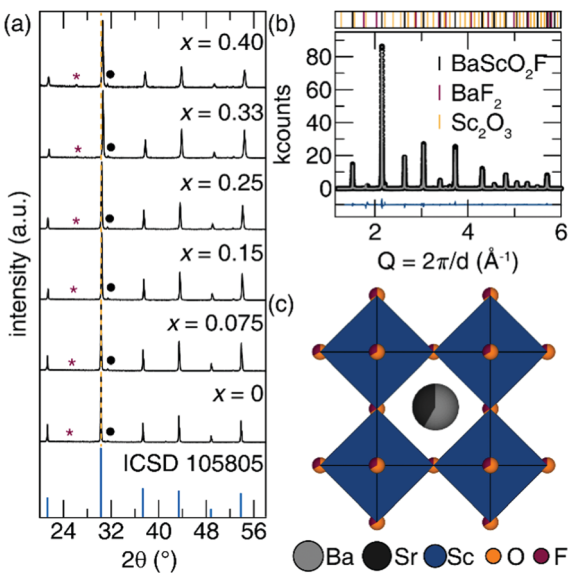

Fig. 1 (a) Powder X-ray diffractograms of $(Ba_{1-x}Sr_x)_{0.98}Eu_{0.02}ScO_2F$ (x = 0, 0.075, 0.15, 0.25, 0.33, 0.40). BaF_2 and Sc_2O_3 impurities are marked with a red asterisk and a black dot, respectively. (b) Synchrotron refinement of $Ba_{0.566(2)}Sr_{0.433(8)}ScO_2F$. The impurity phases were included in the refinement; the refined mole fractions of both impurity phases were less than 5 mol%. (c) The refined perovskite crystal structure of $Ba_{0.566(2)}Sr_{0.433(8)}ScO_2F$.

3.2 The effect of Sr^{2+} substitution on the electronic structure

Density functional theory (DFT) calculations were performed to investigate the structural and electronic changes arising from the gradual substitution of Sr^{2+} in the perovskite crystal structure. To enumerate all possible O/F configurations, all irreducible representations of the $Pm\bar{3}m$ space group that satisfy the Lifshitz criterion were considered.[40] The two lowest energy configurations adopt space groups $P4/mmm$ and $P4_2/mmc$, with the latter favored by only 5 meV per atom (Fig. S2 and Table S2, ESI†). Therefore, all subsequent studies on compounds containing Sr^{2+} are based on the optimized structure with space group $P4_2/mmc$. The thermodynamic evolution of the computed $Ba_{1-x}Sr_xScO_2F$ (x = 0, 0.09375, 0.15625, 0.25, 0.3125) was analyzed by calculating the energy above the convex hull (E_{hull}). E_{hull} measures the decomposition energy of an inorganic compound with respect to the thermodynamically stable phases in the DFT calculated (0 K) phase diagram. The compositions on the convex hull include $BaScO_2F$, $BaSc_2O_4$, $SrSc_2O_4$ and BaF_2. The gradual substitution of Sr^{2+} into $Ba_{1-x}Sr_xScO_2F$ incrementally increases from 80 meV per atom (x = 0) to 113 meV per atom (x = 0.3125) above the E_{hull}, as plotted in Fig. 2a. The increasing E_{hull} indicates it becomes more energetically unfavorable to incorporate Sr^{2+} into the $BaScO_2F$ host crystal structure. This is consistent with the experimentally observed 40% solubility limit of Sr^{2+} and the formation of the $SrSc_2O_4$ impurity phase.

Table 1 Rietveld refinement results obtained using synchrotron X-ray diffraction

Composition	$Ba_{0.566(2)}Sr_{0.433(8)}ScO_2F$
Radiation type, λ (Å)	Synchrotron; 0.457868
2θ range (deg)	0.5–50
Temperature (K)	100
Crystal system	Cubic
Space group; Z	$Pm\bar{3}m$; 1
Lattice parameters (Å)	4.1282(1)
Volume (Å^3)	70.352(2)
R_p	0.0948
R_{wp}	0.1530
χ^2	14.19

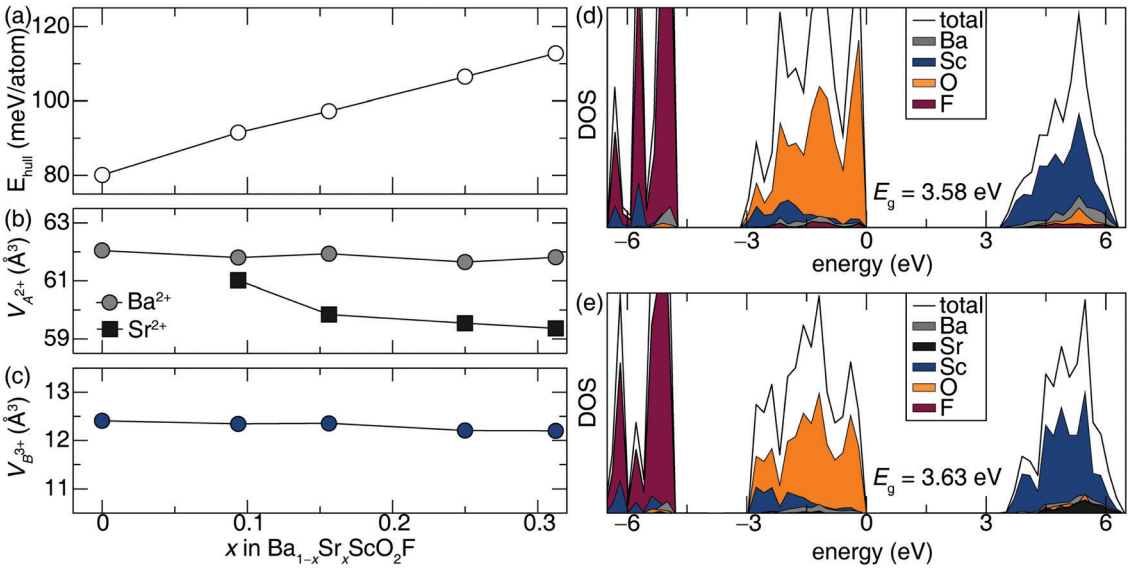

Fig. 2 (a) The DFT computed E_{hull} in $Ba_{1-x}Sr_xScO_2F$, where x = 0, 0.09375, 0.15625, 0.25, 0.3125. The computed polyhedron volume change around (b) Ba^{2+} and Sr^{2+}, the A^{2+} site, and (c) Sc^{3+}, the B^{3+} site, as a function of x. The element-projected density of states of (d) $BaScO_2F$ and (e) $Ba_{0.6875}Sr_{0.3125}ScO_2F$ show a relatively unchanging band gap upon Sr^{2+} insertion.

Substituting Sr^{2+} for Ba^{2+} (and *vice versa*) is a well-known mechanism to shift the photoluminescence of phosphors. However, the structural mechanism to achieve a tunable emission can vary. For example, substituting the smaller Sr^{2+} for the larger Ba^{2+} decreases the average bond length and polyhedral volume of the (Ba/Sr) polyhedral units. This is observed in $Ba_{2-x}Sr_xSiO_4$:Eu^{2+}, $(Ba_{1-x}Sr_x)_{8.46}(Ce_{0.27}Li_{0.27})Sc_2Si_6O_{24}$, and $(Ba_{1-x}Sr_x)Si_3O_4N_2$:Eu^{2+}, among other examples, where the substitution of Sr^{2+} onto the rare-earth substitution site causes a red-shift in the observed emission spectrum.[9,41,42] There are also instances, such as in SrY_2O_4:Eu^{2+}, where the substitution of Ba^{2+} for Sr^{2+}, red-shifts the observed emission. This is counterintuitive but it can be understood because Eu^{2+} preferentially substitutes onto the Y^{3+} sites in the host crystal structure. The mechanism for the red-shift involves the $[SrO_8]$ polyhedral volumes increasing upon Ba^{2+} substitution which contracts the surrounding $[YO_6]$ octahedra to increases the crystal field splitting and induce a red-shift in the emission.[43] This phenomenon is also seen in the $Sr_{1.8}Ba_{0.2}Sc_{0.5}Ga_{1.5}O_5$:$Eu^{2+}$ phosphor.[44] As a result, it is imperative to understand how the $[BaO_{12}]$, $[SrO_{12}]$, and $[ScO_6]$ polyhedral volumes evolve upon the substitution of Sr^{2+} in the $BaScO_2F$ host crystal structure. Structurally, the DFT optimized $Ba_{1-x}Sr_xScO_2F$ (x = 0.0, 0.09375, 0.15625, 0.25, 0.3125) host crystal structure shows minor changes in the $[Ba(O/F)_{12}]$ and $[Sc(O/F)_6]$ polyhedral volumes, seen in Fig. 2b and c, respectively, whereas the polyhedral volume around Sr^{2+} (black square) continuously decreases with increasing x, as shown in Fig. 2b. This computed structural evolution agrees well with the trends in the experimentally measured lattice parameters. The computed decreasing $[SrO_{12}]$ and unchanging $[ScO_6]$ and $[BaO_{12}]$ polyhedral volumes suggest that the crystal field splitting will increase and red-shift the emission spectra of $(Ba_{1-x}Sr_x)_{0.98}Eu_{0.02}ScO_2F$ upon increasing Sr^{2+} concentration.

Electronically, the gradual insertion of Sr^{2+} into $Ba_{1-x}Sr_xScO_2F$ has a minor effect on the band structure. The PBE-level calculated density of states (DOS) shows relatively constant band gap (E_g) between $BaScO_2F$ (E_g = 3.58 eV) and $Ba_{0.6875}Sr_{0.3125}ScO_2F$ (E_g = 3.63 eV), plotted in Fig. 2d and e, respectively. The DOS of the other compounds analyzed (x = 0.09375, 0.15625, 0.25) are provided in Fig. S3 (ESI†). The element-projected DOS reveals that oxygen sets the valence band maximum (VBM) whereas Sc^{3+} 3d orbitals set the conduction band minimum (CBM). Consequently, the uniformity of the O^{2-} and Sc^{3+} band positions arising from the uniformity of the $[Sc(O/F)_6]$ octahedra across the $Ba_{1-x}Sr_xScO_2F$ solid solution yields a nearly constant E_g regardless of Sr^{2+} concentration.

Finally, the average structural rigidity across the solid solution was investigated through Debye temperature calculations. The DFT calculated Debye temperature, $\Theta_{D,DFT}$, was determined for $Ba_{1-x}Sr_xScO_2F$ when x = 0 and 0.3125 to approximate the structural rigidity as a function of composition. Interestingly, the Debye temperature remains nearly constant across the solid solution, exhibiting only a 7 K difference between x = 0 ($\Theta_{D,DFT}$ = 497 K) and x = 0.3125 ($\Theta_{D,DFT}$ = 504 K). This indicates that the average structural rigidity is preserved upon Sr^{2+} substitution. Since the Debye temperature is considered a proxy for the photoluminescent quantum yield (PLQY) of rare-earth substituted phosphors, this suggests the 80% quantum yield of $BaScO_2F$:Eu^{2+} should be retained.[45,46]

3.3 Photoluminescence

$BaScO_2F$:Eu^{2+} is a phosphor that produces a bright cyan emission with a maximum PLQY of 80.3(5)% with 2% Eu^{2+} substitution.[20] For the study here, the rare-earth substitution concentration was held constant as Sr^{2+} was incrementally introduced into the host crystal structure following the general formula $(Ba_{1-x}Sr_x)_{0.98}Eu_{0.02}ScO_2F$ (x = 0.075, 0.15, 0.25, 0.33, and 0.40).

The resulting excitation spectra are plotted in Fig. 3a. Each phosphor in the solid solution possesses a wide excitation band covering approximately 280 nm to 450 nm with three distinct maxima as provided in Table 2. The maxima of the excitation bands indicate excellent compatibility with UV LEDs.

The emission spectra under 340 nm excitation, also shown in Fig. 3a, covers a broad region from 400 nm to 700 nm, where the emission peak maxima shifts from 481 nm ($x = 0$) to 516 nm ($x = 0.40$). This red-shift is reflected in the 1931 CIE *XYZ* coordinates of the solid solution, where the perceived emission color linearly shifts from cyan to green, indicating successful tunability of the observed emission color (Fig. 3b). Each phosphor's emission color is not saturated due to the broad full width at half maximum (fwhm) across the solid solution. Indeed, the fwhm of the emission peak falls between 100 nm and 107 nm (4158–4420 cm^{-1}). Such a broad emission is inherent to the perovskite crystal structure of $BaScO_2F:Eu^{2+}$, which possesses two crystallographically independent Eu^{2+} atoms upon rare-earth substitution, as discussed previously.[20] As a result, the emission spectrum of $BaScO_2F:Eu^{2+}$ ($x = 0$) is described by two distinct Gaussians to represent the emission from the independent Eu^{2+} atoms, illustrated in blue in Fig. 3a. The optical properties shown here indicate the gradual substitution of Sr^{2+} in $BaScO_2F:Eu^{2+}$ preserves the emission peak shape while red-shifting the emission. This suggests the local Eu^{2+} coordination environments across the solid solution are maintained, while Sr^{2+} substitution decreases the polyhedral volume (Fig. 2b), leading to the observed red-shift in the emission spectra. Additionally, there is little change between the fwhm of each emission peak, suggesting the magnitude of electron–phonon coupling is not affected by Sr^{2+} substitution (Table 2).[47] This broad emission is ultimately advantageous in producing a full-spectrum white light by covering the blue, cyan, and green regions of the visible spectrum.

Table 2 Photoluminescence properties of $(Ba_{1-x}Sr_x)_{0.98}Eu_{0.02}ScO_2F$ ($x = 0$, 0.075, 0.15, 0.25, 0.33, 0.40)

	λ_{ex} (nm)	$\lambda_{em,max}$ (nm)	fwhm
$x = 0$	282, 340, 365	487	103 nm, 4228 cm^{-1}
$x = 0.075$	279, 341, 369	496	103 nm, 4158 cm^{-1}
$x = 0.15$	276, 340, 371	504	100 nm, 4420 cm^{-1}
$x = 0.25$	272, 342, 372	509	105 nm, 4251 cm^{-1}
$x = 0.33$	267, 339, 372	512	102 nm, 4378 cm^{-1}
$x = 0.40$	265, 340, 373	516	107 nm, 4328 cm^{-1}

The observed red-shift in the emission spectrum is further supported by analyzing the crystallographic site preference for Eu^{2+} to substitute for Ba^{2+} or Sr^{2+} within the crystal structure. Rietveld refinements cannot accurately probe the Eu^{2+} location due to its low substitution concentration (2%). Instead, the site preference was determined by calculating the dopant formation energies of $Ba_{1-x}Sr_xScO_2F$ ($x = 0$, 0.09375, 0.15625, 0.25, 0.3125). These models used $2 \times 4 \times 4$ supercells and a constant Eu^{2+} concentration of 3% substituted onto either the Ba^{2+} site (Eu_{Ba}) or the Sr^{2+} site (Eu_{Sr}). The resulting dopant formation energy difference between Eu_{Ba} and Eu_{Sr} for $x < 0.25$ is relatively constant, $\approx$1.85 meV per atom favoring Eu_{Sr}. This value decreases to $\approx$0.9 meV per atom when $x = 0.3125$ but still indicates that Eu^{2+} should preferentially substitute for Sr^{2+} (Fig. S4, ESI†). Analyzing the DFT optimized $Ba_{1-x}Sr_xScO_2F:Eu^{2+}$ ($x = 0$, 0.09375, 0.15625, 0.25, 0.3125) models show the average bond length forming the Eu^{2+} coordination polyhedron as a function of Sr^{2+} gradually decreases (Table S3, ESI†), which increases the crystal field splitting around Eu^{2+} and inherently induces the observed red-shifted emission generating the green emission.

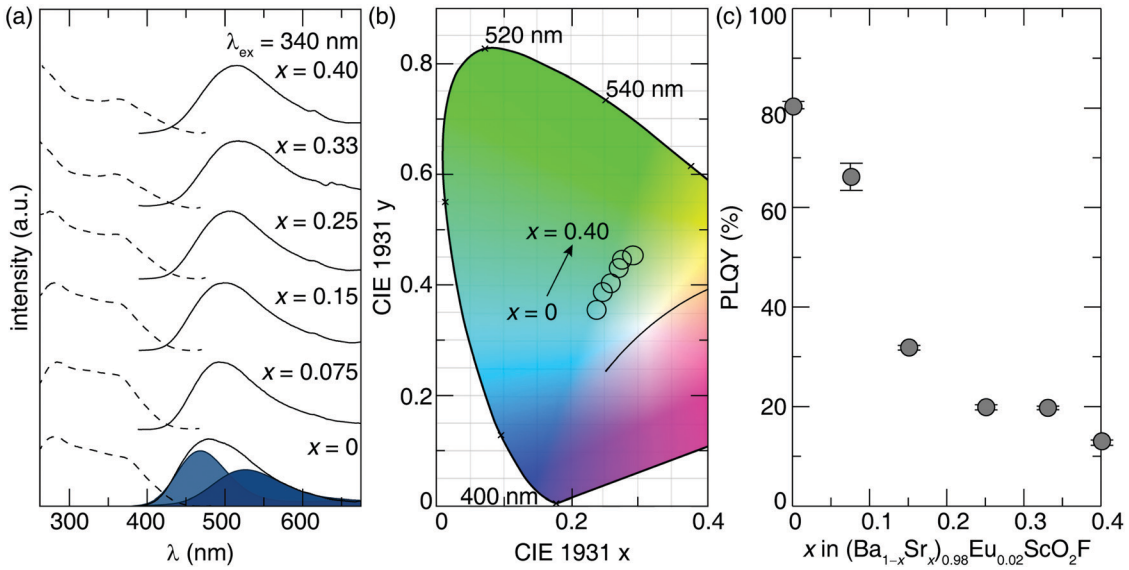

Fig. 3 (a) Excitation spectrum (dashed line) and emission spectrum (solid line) where the two blue Gaussian peaks represent the emission from two crystallographically independent Eu^{2+} sites, (b) CIE coordinates, and (c) room temperature PLQY of $(Ba_{1-x}Sr_x)_{0.98}Eu_{0.02}ScO_2F$ ($x = 0$, 0.075, 0.15, 0.25, 0.33, and 0.40).

Even though a novel phosphor may emit in the desired color range, integration into LED light bulbs requires efficient photoluminescence. Therefore, the room temperature PLQY was measured to determine whether the high (80.3(5)%) quantum yield of $Ba_{0.98}Eu_{0.02}ScO_2F$ was maintained. The room temperature PLQY of $(Ba_{1-x}Sr_x)_{0.98}Eu_{0.02}ScO_2F$ (x = 0.075, 0.15, 0.25, 0.33, 0.40) was determined using an excitation wavelength of 340 nm and plotted in Fig. 3c. Incorporating 7.5% Sr^{2+} causes the PLQY to decrease to 66.1(6)%. Doubling the Sr^{2+} concentration to 15% causes the efficiency to decrease by more than half (PLQY = 31.7(9)%), and substituting 40% Sr^{2+} into the structure results in a dramatic drop in the PLQY to 12.7(5)%. This result is surprising because the nearly constant Debye temperature suggests a minimal change in the PLQY should occur as a function of Sr^{2+} concentration.

The change in room temperature PLQY could stem from a variety of different sources. The minor presence of the Eu^{3+} 4f ↔ 4f emission around 605 nm at higher Sr^{2+} concentrations (Fig. 3a) can cause a drop in the PLQY. However, the Eu^{3+} as a luminescence quencher in the solid solution appears to be constant based on the intensity of these emission peaks. Thus, the presence of the trivalent rare-earth does not fully explain the dramatic drop in the PLQY with increasing Sr^{2+}. Additionally, the decrease in the PLQY may be related to the temperature-dependence photoluminescence. The optical properties of rare-earth substituted phosphors can change considerably as a function of temperature. One of the most notable changes is a loss of photoluminescence emission intensity known as thermal quenching (TQ). Thus, the substitution of Sr^{2+} could cause an increase in TQ at room temperature that decreases the PLQY.

3.4 Thermal quenching and its relationship to local environment rigidity

Measuring the photoluminescent emission spectrum of each phosphor from 80 K to 500 K and plotting the normalized, integrated intensity as a function of the temperature range in Fig. 4a shows $BaScO_2F:Eu^{2+}$ remains stable up to 260 K and begins to quench with increasing temperature. Adding Sr^{2+} in the phosphors causes thermal quenching to begin beyond 220 K, resulting in a ≈25% drop in the integrated emission intensity by room temperature (300 K), shown as the solid black line in Fig. 4a. This behavior is reflected in all of the phosphors across the solid solution. By room temperature, the Sr^{2+}-substituted phosphors are already undergoing different rates of thermal quenching, causing a drop in photoluminescence intensity, which is responsible for the observed decrease in the PLQY.

It is well understood that thermal quenching is accompanied by a decrease of the photoluminescence decay time, τ.[48,49] Therefore, the time-resolved room temperature photoluminescent decay curve was measured under 330 nm excitation. The photoluminescent lifetime was determined by fitting the decay curve to a bi-exponential following eqn (4), where I is intensity, I_0 is the initial intensity, A_1, and A_2 are the pre-exponential

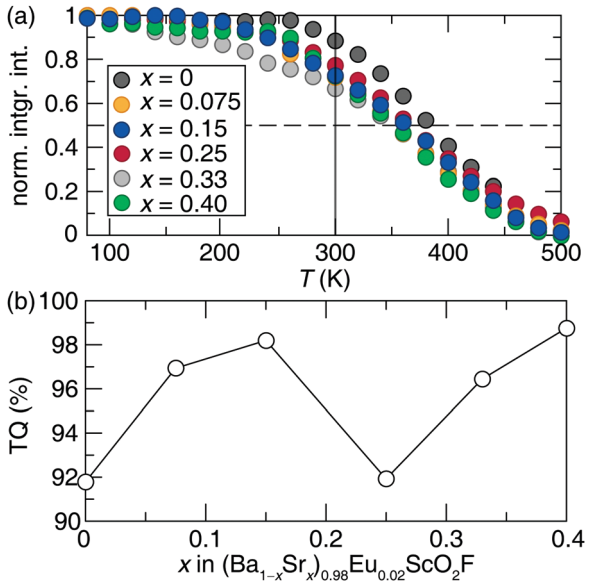

Fig. 4 (a) The normalized, integrated emission intensity as a function of temperature from 80–500 K and (b) the thermal quenching (TQ) of $(Ba_{1-x}Sr_x)_{0.98}Eu_{0.02}ScO_2F$ (x = 0, 0.075, 0.15, 0.25, 0.33, 0.40) expressed as the ratio between the integrated light intensity emitted at 500 K and 300 K.

constants, τ_1 and τ_2 are decay times for exponential components in microseconds, and t is the measured time.

$$I = I_0 + A_1 e^{-t/\tau_1} + A_1 e^{-t/\tau_2} \quad (4)$$

The bi-exponential fit, represented by the solid lines in Fig. S5a (ESI†), captures each decay curve and further corroborates the dual emission across the solid solution. The lifetimes become progressively shorter across the entire range of x, plotted in Fig. S5b (ESI†), with one faster component falling in the range of 0.051 μs to 0.256 μs and one longer component in the range of 0.415 μs to 0.786 μs. The decrease in the decay time as a function of Sr^{2+} concentration is due to the earlier onset of thermal quenching and is consistent with the loss of PLQY at room temperature.

The thermal quenching of each phosphor can also be quantified by defining and plotting the TQ as the ratio between the integrated emission intensity at high temperature (500 K), which is above the operating temperature of most LED-based light bulbs, and room temperature (300 K). Fig. 4b plots the TQ values of $(Ba_{1-x}Sr_x)_{0.98}Eu_{0.02}ScO_2F$ (x = 0, 0.075, 0.15, 0.25, 0.33, 0.40) and depicts an increase in TQ once Sr^{2+} is introduced into the system. This outcome is crucial as it reveals that the substitution of Sr^{2+} into the perovskite structure hinders the thermal stability of the emission. There are multiple TQ mechanisms responsible for the differences in temperature-dependent photoluminescence. One quenching mechanism is related to photoionization, where the excited state electron in the rare-earth 5d orbital transitions to the host conduction band and is subsequently lost. This process becomes a prominent quenching mechanism in phases when the host E_g is decreased as a function of composition.[22] In this system,

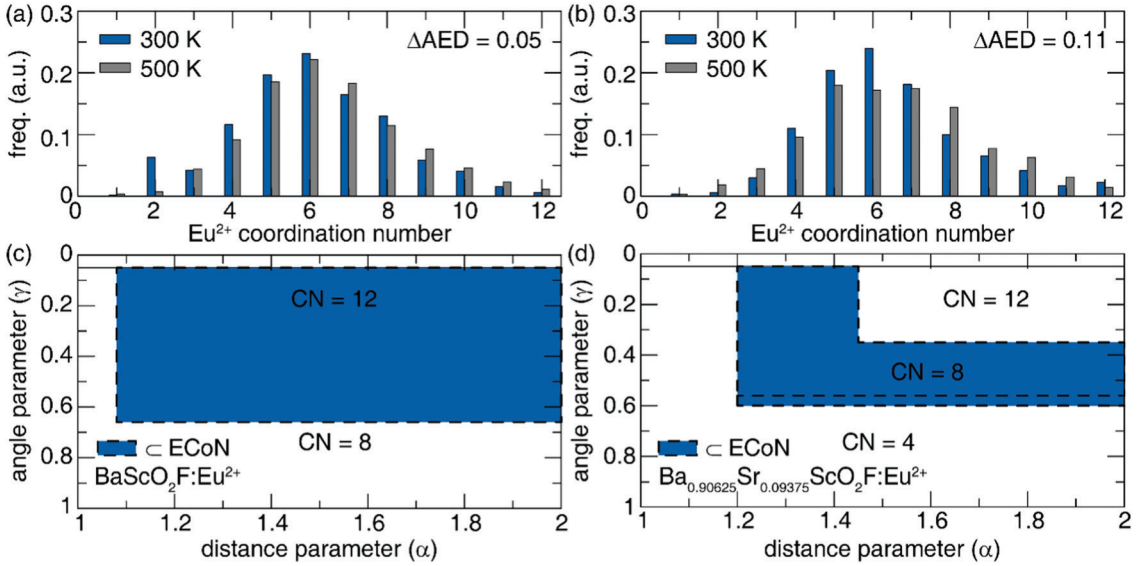

Fig. 5 The Eu^{2+} coordination environment distribution (AED) when (a) $x = 0$ and (b) $x = 0.09375$ in $Ba_{1-x}Sr_xScO_2F:Eu^{2+}$ at 300 K (blue) and 500 K (grey). The Voronoi grid representation of Eu^{2+} local environment of (c) $BaScO_2F:Eu^{2+}$ and (d) $Ba_{0.90625}Sr_{0.09375}ScO_2F:Eu^{2+}$.

however, the magnitude of E_g remains relatively constant as a function of Sr^{2+} (Fig. 2d and e). Previous work has also shown that the thermal quenching of Eu^{2+} substituted phosphors correlates to the phosphor host's structural rigidity, which quantifies the cross-over quenching mechanism.[50] Structural rigidity can be assessed based on the material's measured or calculated Θ_D. Interestingly, the calculated Debye temperatures are nearly constant as a function of composition, ranging from 497 K ($x = 0$) to 504 K ($x = 0.3125$), or $<2\%$ different. The similar structural rigidity also does not provide any additional insight on the TQ response. These analyses in tandem show that these calculated average structure proxies for understanding a phosphor's optical properties are not sufficient for this system.

The local structure around the rare-earth ion must be considered instead. The Eu^{2+} local coordination environment can be investigated by computing the local activator environment distribution (AED) at two temperatures, room temperature and high temperature (300 K and 500 K), using AIMD calculations. Here, the AED is determined by extracting the number of simulations timesteps that the rare-earth forms a particular coordination number (CN). The change in the AED (ΔAED) between 300 K and 500 K is directly correlated with TQ.[22] The calculated shift in AED in the pristine phosphor ($x = 0$) is small (ΔAED = 0.05), whereas the Sr^{2+} substituted phosphor ($x = 0.09375$) shows a larger shift in AED (ΔAED = 0.11) as shown in Fig. 5a and b, respectively. The larger ΔAED indicates that the rare-earth environment is more prone to local polyhedral distortions upon Sr^{2+} substitution. In addition, the larger ΔAED suggests increased TQ, which is experimentally observed in the onset of quenching occurring at lower temperatures yielding lower room temperature PLQY. The local environment rigidity can also be investigated *via* a two-dimensional projection of the Eu^{2+} coordination environment using the Voronoi tessellation representation. Here, a constant, normalized Voronoi area is assumed to be less sensitive to the thermally induced fluctuations and hence, less prone to thermal quenching. Plotting the Voronoi grid representation and highlighting the area of interest around Hoppe's effective rare-earth local environment for $BaScO_2F:Eu^{2+}$ (Fig. 5c) shows the CN is nearly always 12 whereas the CN in $Ba_{0.90625}Sr_{0.09375}ScO_2F:Eu^{2+}$ can be either 12, 8, or 4 (Fig. 5d). This reflects that substituting Sr^{2+} decreases the Eu^{2+} local rigidity indicated by the changing AED, consequently increasing the thermal quenching. These AIMD calculations are the only method that validates the decrease in TQ and PLQY of this new green-emitting phosphor that arises from the substitution of Sr^{2+} in $Ba_{1-x}Sr_xScO_2F:Eu^{2+}$.

4. Conclusion

The development of novel green-emitting phosphors by substituting Sr^{2+} into the $BaScO_2F:Eu^{2+}$ perovskite was successful. The synthesis of the solid solution following $(Ba_{1-x}Sr_x)_{0.98}Eu_{0.02}ScO_2F$ ($x = 0$, 0.075, 0.15, 0.25, 0.40) causes a 30 nm red-shift of the cyan emission of the parent phosphor to the green region of the visible spectrum. However, the high efficiency of the parent phosphor, $Ba_{0.98}Eu_{0.02}ScO_2F$, is not retained across the solid solution, with a nearly 65% decrease in the PLQY when $x = 0.40$. In addition, there is severe thermal quenching observed in this solid solution. Average electronic structure calculations of the band gap and Debye temperature of $Ba_{1-x}Sr_xScO_2F:Eu^{2+}$ ($x = 0$, 0.09375, 0.15625, 0.25, 0.3125) were inadequate to describe the trend in the observed optical properties. Instead, *ab initio* molecular dynamics simulations revealed that a decrease in the local activator environment rigidity is responsible for the increasing TQ and loss of PLQY. These results provide considerable support for using computational

modeling, including standard DFT but more importantly, advanced AIMD calculations, to analyze the average structure and local rare-earth environment as a function of temperature to understand the optical properties of new luminescent materials.

Conflicts of interest

The authors declare no competing financial interest.

Acknowledgements

S. H., M. K., and J. B. would like to thank the National Science Foundation (CER-1911311) as well as the Welch Foundation (E-1981) for supporting this work. M. A. and S. P. O. also acknowledge funding from the National Science Foundation (CER-1911372), computing resources provided by the National Energy Research Scientific Computing Center (NERSC) under Contract No. DE-AC02-05CH11231 using NERSC award BES-ERCAP0018251, the Triton Shared Computing Cluster (TSCC) at the University of California, San Diego, and the Extreme Science and Engineering Discovery Environment (XSEDE) under grant ACI-1548562. This work used the resources available through the 11-BM beamline at the Advanced Photon Source, an Office of Science User Facility operated for the US Department of Energy (DOE) Office of Science by Argonne National Laboratory, under Contract No. DE-AC02-06CH11357.

References

1 U. S. Department of Energy, Energy Saver, https://www.energy.gov/energysaver/led-lighting, (accessed September, 2021).
2 P. Pust, P. J. Schmidt and W. Schnick, *Nat. Mater.*, 2015, **14**, 454–458.
3 J. Hye Oh, S. Ji Yang and Y. Rag Do, *Light Sci. Appl.*, 2014, **3**, e141.
4 M.-H. Fang, C. Ni, X. Zhang, Y.-T. Tsai, S. Mahlik, A. Lazarowska, M. Grinberg, H.-S. Sheu, J.-F. Lee, B.-M. Cheng and R.-S. Liu, *ACS Appl. Mater. Interfaces*, 2016, **8**, 30677–30682.
5 P. Pust, V. Weiler, C. Hecht, A. Tücks, A. S. Wochnik, A.-K. Henß, D. Wiechert, C. Scheu, P. J. Schmidt and W. Schnick, *Nat. Mater.*, 2014, **13**, 891–896.
6 S. Li, Y. Xia, M. Amachraa, N. T. Hung, Z. Wang, S. P. Ong and R.-J. Xie, *Chem. Mater.*, 2019, **31**, 6286–6294.
7 S. Li, L. Wang, D. Tang, Y. Cho, X. Liu, X. Zhou, L. Lu, L. Zhang, T. Takeda, N. Hirosaki and R.-J. Xie, *Chem. Mater.*, 2018, **30**, 494–505.
8 K. Park, T. Kim, Y. Yu, K. Seo and J. Kim, *J. Lumin.*, 2016, **173**, 159–164.
9 K. A. Denault, J. Brgoch, M. W. Gaultois, A. Mikhailovsky, R. Petry, H. Winkler, S. P. DenBaars and R. Seshadri, *Chem. Mater.*, 2014, **26**, 2275–2282.
10 Y. Zhuo, S. Hariyani, J. Zhong and J. Brgoch, *Chem. Mater.*, 2021, **33**, 3304–3311.
11 Y. Ohno, Color Rendering and Luminous Efficacy of White LED Spectra, SPIE, 2004.
12 M. Zhao, Q. Zhang and Z. Xia, *Acc. Mater. Res.*, 2020, **1**, 137–145.
13 P. D. Rack and P. H. Holloway, *Mater. Sci. Eng., R*, 1998, **21**, 171–219.
14 Z. Xia, Q. Li and J. Sun, *Mater. Lett.*, 2007, **61**, 1885–1888.
15 X. Zhang, X. Wang, J. Huang, J. Shi and M. Gong, *Opt. Mater.*, 2009, **32**, 75–78.
16 K. A. Denault, N. C. George, S. R. Paden, S. Brinkley, A. A. Mikhailovsky, J. Neuefeind, S. P. DenBaars and R. Seshadri, *J. Mater. Chem.*, 2012, **22**, 18204–18213.
17 W. B. Im, S. Brinkley, J. Hu, A. Mikhailovsky, S. P. DenBaars and R. Seshadri, *Chem. Mater.*, 2010, **22**, 2842–2849.
18 W. B. Im, N. George, J. Kurzman, S. Brinkley, A. Mikhailovsky, J. Hu, B. F. Chmelka, S. P. DenBaars and R. Seshadri, *Adv. Mater.*, 2011, **23**, 2300–2305.
19 M. Hermus, P.-C. Phan, A. C. Duke and J. Brgoch, *Chem. Mater.*, 2017, **29**, 5267–5275.
20 S. Hariyani and J. Brgoch, *Chem. Mater.*, 2020, **32**, 6640–6649.
21 U. S. Department of Energy, Solid-State Lighting Research and Development Multi-Year Program Plan, https://www1.eere.energy.gov/buildings/publications/pdfs/ssl/ssl_mypp2014_web.pdf, (accessed October, 2021).
22 M. Amachraa, Z. Wang, C. Chen, S. Hariyani, H. Tang, J. Brgoch and S. P. Ong, *Chem. Mater.*, 2020, **32**, 6256–6265.
23 B. H. Toby, *J. Appl. Crystallogr.*, 2001, **34**, 210–213.
24 K. Momma and F. Izumi, *J. Appl. Crystallogr.*, 2011, **44**, 1272–1276.
25 J. C. de Mello, H. F. Wittmann and R. H. Friend, *Adv. Mater.*, 1997, **9**, 230–232.
26 G. L. W. Hart and R. W. Forcade, *Phys. Rev. B: Condens. Matter Mater. Phys.*, 2008, **77**, 224115.
27 S. P. Ong, S. Cholia, A. Jain, M. Brafman, D. Gunter, G. Ceder and K. A. Persson, *Comput. Mater. Sci.*, 2015, **97**, 209–215.
28 G. Kresse and J. Furthmüller, *Phys. Rev. B: Condens. Matter Mater. Phys.*, 1996, **54**, 11169–11186.
29 A. Chaudhry, R. Boutchko, S. Chourou, G. Zhang, N. Grønbech-Jensen and A. Canning, *Phys. Rev. B: Condens. Matter Mater. Phys.*, 2014, **89**, 155105.
30 S.-H. Wei and S. B. Zhang, *Phys. Rev. B: Condens. Matter Mater. Phys.*, 2002, **66**, 155211.
31 Z.-J. Wu, E.-J. Zhao, H.-P. Xiang, X.-F. Hao, X.-J. Liu and J. Meng, *Phys. Rev. B: Condens. Matter Mater. Phys.*, 2007, **76**, 054115.
32 W. G. Hoover, *Phys. Rev. A: At., Mol., Opt. Phys.*, 1985, **31**, 1695–1697.
33 A. S. Bhalla, R. Guo and R. Roy, *Mater. Res. Innovations*, 2000, **4**, 3–26.
34 R. L. Needs and M. T. Weller, *J. Solid State Chem.*, 1998, **139**, 422–423.
35 R. D. Shannon and C. T. Prewitt, *Acta Crystallogr., Sect. B: Struct. Sci.*, 1969, **25**, 925–946.
36 E.-a. Zen, *Am. Mineral.*, 1956, **41**, 523–524.

37 M. Müller, M.-F. Volhard and T. Jüstel, *RSC Adv.*, 2016, **6**, 8483–8488.
38 K. S. Aleksandrov and J. BartolomÉ, *Phase Transitions*, 2001, **74**, 255–335.
39 R. L. Needs and M. T. Weller, *J. Solid State Chem.*, 1998, **139**(2), 422–423.
40 M. V. Talanov, V. B. Shirokov and V. M. Talanov, *Acta Crystallogr., Sect. A: Found. Crystallogr.*, 2016, **72**, 222–235.
41 J. Brgoch, C. K. H. Borg, K. A. Denault, S. P. DenBaars and R. Seshadri, *Solid State Sci.*, 2013, **18**, 149–154.
42 Z. Zhang and W. Yang, *Opt. Mater. Express*, 2019, **9**, 1922–1932.
43 Z. Yang, Y. Zhao, Y. Zhou, J. Qiao, Y.-C. Chuang, M. S. Molokeev and Z. Xia, *Adv. Funct. Mater.*, 2022, **32**, 2103927.
44 Z. Yang, Y. Zhou, J. Qiao, M. S. Molokeev and Z. Xia, *Adv. Opt. Mater.*, 2021, **9**, 2100131.
45 J. Brgoch, S. P. DenBaars and R. Seshadri, *J. Phys. Chem. C*, 2013, **117**, 17955–17959.
46 S. Hariyani, A. C. Duke, T. Krauskopf, W. G. Zeier and J. Brgoch, *Appl. Phys. Lett.*, 2020, **116**, 051901.
47 G. Blasse, *Structure and Bonding*, Springer, Berlin, Heidelberg, 1980, vol. 42.
48 D. Van der Heggen, J. J. Joos and P. F. Smet, *ACS Photonics*, 2018, **5**, 4529–4537.
49 V. Bachmann, C. Ronda and A. Meijerink, *Chem. Mater.*, 2009, **21**, 2077–2084.
50 Y. Zhuo, A. Mansouri Tehrani, A. O. Oliynyk, A. C. Duke and J. Brgoch, *Nat. Commun.*, 2018, **9**, 4377.

